J. Cent. South Univ. (2020) 27: 2883−2898
DOI: https://doi.org/10.1007/s11771-020-4516-6

Springer

Acoustic emission precursors of static and dynamic instability for coarse-grained hard rock

SU Guo-shao(苏国韶), GAN Wei(甘伟), ZHAI Shao-bin(翟少彬), ZHAO Guo-fu(赵国富)

Key Laboratory of Disaster Prevention and Structural Safety of Ministry of Education, School of Civil Engineering and Architecture, Guangxi University, Nanning 530004, China

Abstract: To investigate the acoustic emission (AE) precursors of coarse-grained hard rock instability, an experimental study on the rockburst and slabbing process of granite was carried out using a true triaxial test system. The evolution of the AE signals was monitored and analyzed in terms of the AE hit rate, fractal dimension of the AE hit number, AE count rate, *b*-value, dominant frequency and microcrack type. The test results show that after rock slabbing occurs, the AE precursors that can be used to predict the final dynamic instability (rockburst) are as follows: indicators such as the AE hit rate and AE count rate suddenly increase and then suddenly decrease; the AE hit rate exhibits a "quiet period"; during the "quiet period", a small number of high-amplitude and low-frequency hits occur, and the signals corresponding to shear fracture continue to increase. The AE precursors for the final static instability (spalling) are as follows: both the AE hit rate and the *b*-value continuously decrease, and intermittent sudden increases appear in the high-frequency hits or the AE count rate.

Key words: rockburst; slabbing; spalling; acoustic emission; true triaxial test

Cite this article as: SU Guo-shao, GAN Wei, ZHAI Shao-bin, ZHAO Guo-fu. Acoustic emission precursors of static and dynamic instability for coarse-grained hard rock [J]. Journal of Central South University, 2020, 27(10): 2883−2898. DOI: https://doi.org/10.1007/s11771-020-4516-6.

1 Introduction

Rockburst and spalling are the most common geological disasters in deep hard rock engineering [1]. Rockburst, a dynamic instability phenomenon (Figure 1(a)), is characterized by fragments ejecting away from the surrounding rock, while spalling is characterized by thin plate-shaped rocks spalling from the surrounding rocks, belonging to the static instability phenomenon (Figure 1(b)). Both rockburst and spalling can directly threaten the safety of construction personnel and affect project progress [2−4]. Therefore, it is urgent to improve the prediction and warning of rockburst and spalling.

Previous field experience and indoor studies have shown that slabbing is an inevitable and precursor process for strainburst in intact rocks around deep tunnels [5−7]. Historically, the phenomenon of rock slabbing has often been used to provide a warning for rockburst failure. However, it should be pointed out that slabbing failure does not indicate that the occurrence of rockburst is inevitable. This is because after rock slabbing, two distinct modes of instability may appear. One mode of instability is static spalling instability, which is characterized by slabs falling after buckling and breaking. Another is dynamic rockburst instability characterized by the violent ejection of fragments after slabs break and fracture. For example, in the diversion tunnel of the

Foundation item: Project(51869003) supported by the National Natural Science Foundation of China; Project(T3030097958) supported by the High Level Innovation Team and Outstanding Scholar Program of Universities in Guagnxi Province, China
Received date: 2020-06-12; **Accepted date:** 2020-08-13
Corresponding author: SU Guo-shao, PhD, Professor; Tel: +86-7713232894; E-mail: guoshaosu@gxu.edu.cn; ORCID: https://orcid.org/0000-0001-9506-6827

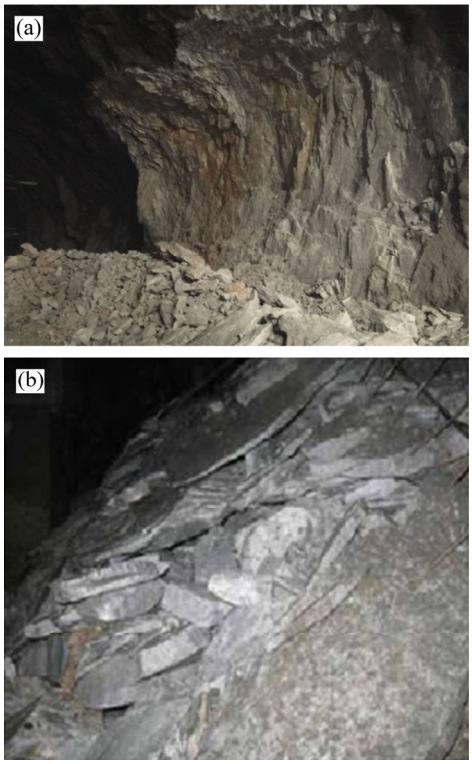

Figure 1 Rock instability in the tunnel of Jinping II Hydropower Station, China, of: (a) Rockburst; (b) Spalling [8, 9]

Jinping II Hydropower Station, China, spalling and rockburst are the two most common brittle failure phenomena (see Figure 1) [4]. An important and difficult problem encountered on the site was how to provide a warning for the final instability mode of the surrounding rock according to the evolution characteristics of acoustic emission (AE) signals after rock slabbing. It is unclear whether the static spalling instability of the slab breaking off and falling or the dynamic instability of rockburst will occur.

Acoustic emissions proceeding in the hard rock fracture process contains rich information and has been widely used in rock instability prediction and warning. Specifically, the evolution characteristics of AE parameters are critical for the prediction and the early warning of the instability of the surrounding rock.

Since the discovery of the Kaiser effect in AE monitoring [10, 11], the study of the AE evolution characteristics in rocks has received considerable interest and attention in the field of rock mechanics and engineering. For the time-domain characteristics of AEs, RUDAJEV et al [12] studied the precursors of rock failure under uniaxial compression and pointed out that the time series of AEs would change suddenly before rock failure. CHMEL et al [13] found the phenomenon of the AE “quiet period” before the instability of granite samples under both continuous compression and impact loading [13].

MORADIAN et al [14] used the characteristics of AE parameters to analyze the cracking process in granite containing structural planes under uniaxial loading. TRIANTIS [15] found that when the rock sample approached failure, the *b*-value decreased rapidly, average frequency (AF) decreased, and rise time/amplitude ratio ralue (RA) increased, indicating that the rock failure was dominated by shear failure. SELAHATTIN et al [16] used AE technology to study the failure characteristics of hard brittle rocks under true triaxial conditions. It was found that the *b*-value showed a continuous decrease before rockburst and thus could be used as a precursor of rock failure.

For the frequency domain characteristics of AEs, MORADIAN et al [17] conducted a uniaxial compression test on coal-rock mixed samples and found that the dominant frequency band became wider, and the AEs exhibited obvious low-frequency characteristics when rockburst occurred. The lower the dominant frequency, the higher the energy of the corresponding AEs and the more violent the rockburst. The low frequency phenomenon could be used to predict rockbursts. HE et al [18, 19] found that the rate of the AE events and the AE energy at the instant of rockburst failure increased sharply. The AE spectrum characteristics were substantially different between the tensile and shear fractures.

In terms of the fractal characteristics of AEs, HIMURA et al [20] found that the *b*-value and the fractal dimension of the AEs changed consistently during rock failure. KONG et al [21] indicated that the reduction in the AE fractal dimension could be used as the precursor information of sample instability. ZHANG et al [22] noted the obvious reduction in the AE spatial fractal dimension under uniaxial compression that could be used as a precursor of rock failure. However, the above research did not indicate whether spalling or rockburst would occur when these precursor characteristics appeared. This was also a source of concern for engineers in terms of the early warning of rockburst using AE signals.

In this study, we conducted true triaxial tests of rockburst and spalling by controlling different loading rates on a coarse-grained granite material. The AE characteristic parameters, such as the AE hit rate, amplitude, time fractal dimension of the AE hit number, AE count rate, *b*-value, dominant frequency, and tensile/shear fracture ratio, are analyzed and compared during the process of rockburst and static instability after slabbing. This work can help to solve the problem associated with prediction of the final instability mode of the surrounding rock using AE signals in deep rock engineering applications.

2 Experimental methodology

The tests are conducted on a novel self-developed true triaxial rockburst testing system (Figure 2), which mainly includes a true triaxial rockburst testing machine, an AE monitoring system, a high-speed camera system, lighting facilities, and physical measurement devices. The true triaxial testing machine can independently apply a load in three orthogonal directions using solid pistons, with the maximum loading capacity of 5000 kN in the vertical direction and 3000 kN in the horizontal direction. The testing machine can simulate a variety of complex stress and boundary conditions, such as true triaxial loading, one-face free true triaxial loading, and biaxial loading.

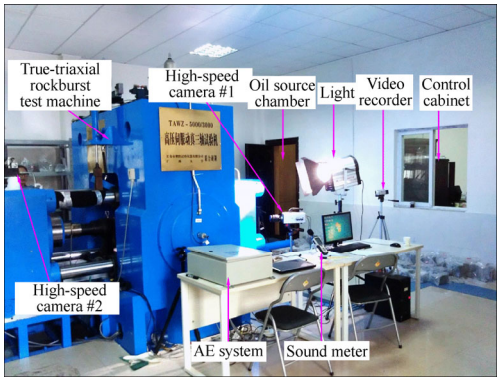

Figure 2 True-triaxial rockburst testing system [23]

The tested rock material is a coarse-grained granite material from Wuzhou, China (Figure 3). The dimensions of the rectangular prismatic sample are 200 mm×100 mm×100 mm. The granite has good integrity and homogeneity, and the *P* wave velocity is approximately 5200 m/s at normal temperatures. The density is approximately 2607 kg/m³; the average uniaxial compressive strength is approximately 120 MPa; the elastic modulus is approximately 34.25 GPa; and the Poisson ratio is approximately 0.2.

Figure 3 Granite samples

The rockburst and spalling induced by the tangential stress concentration after excavation and unloading of the radial stress around the deep tunnel are simulated and investigated [24−26]. The tests are conducted following a load path of "one face free-five faces loaded-keeping loading vertically" (Figure 4), which includes the following loading scheme: maintaining a free surface and loading the minimum principal stress σ_3 to 5 MPa on the opposite surface (after excavation, the radial stress decreases sharply, but a small radial stress gradient can exist); loading the intermediate

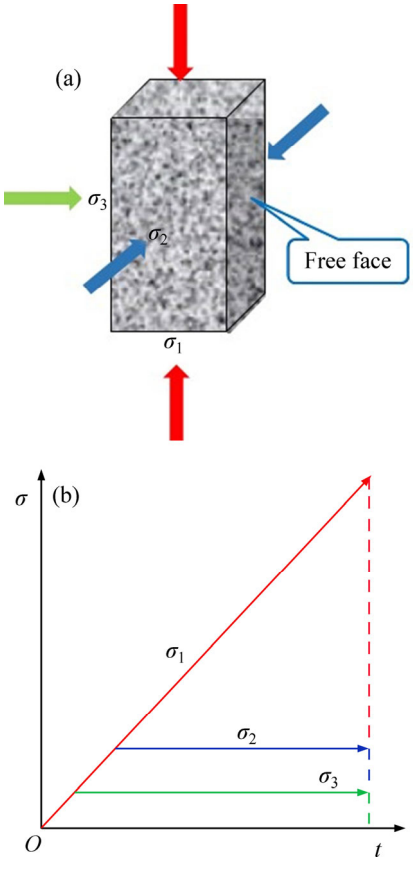

Figure 4 (a) Stress state; (b) Loading path of tests [7]

principal stress σ_2 to 30 MPa; and loading the axial stress σ_1 at a rate of 1.2 and 0.05 MPa/s in the rockburst and spalling tests, respectively [27], until the failure of the specimen.

The AE signal is monitored using the AE system from Physical Acoustics Corporation . The system has a total of sixteen high-speed acquisition channels, three of which are selected in the tests. The sampling rate is set to 1 million samples per second (MSPS), and the threshold is set to 40 dB. In the tests, three AE probes are arranged on the base platen. To ensure coupling, butter is used as a couplant (Figure 5), verified by experiment that the arrangement of the probe will not affect the trend of the AE signal.

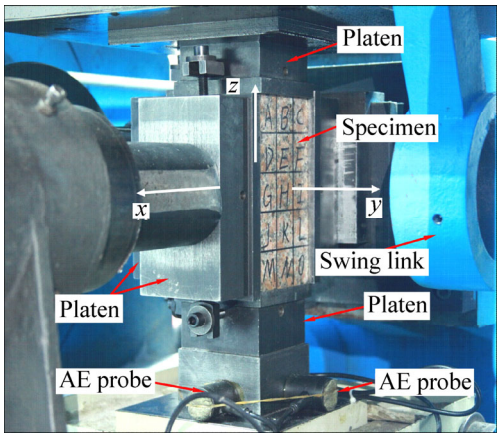

Figure 5 Arrangement of AE sensors [7]

3 AE hit rate evolution

3.1 AE Hit rate evolution during rockburst and spalling

The AE hit rate, as an important characteristic parameter, can reflect the activity of the AE and the strength of cracking inside the rock.

The temporal changes in the AE hit rate during the rockburst test are shown in Figure 6, along with the failure phenomena recorded by the video. As shown in Figure 6, during 1−50 s, the AE hit rate increases first and then decreases, with the maximum of 210. During 50−182 s, the AE hit rate enters the active period and gradually increases, up to approximately 110. In the corresponding video image, small cracks and particle ejection occur on the free surface. At 183 s, the AE hit rate increases sharply, up to 90. Slabbing begins to appear on the free face of the rock sample. At 189 s, the AE hit rate continues to increase, up to 130. Obvious slabbing appears again on the free surface of the

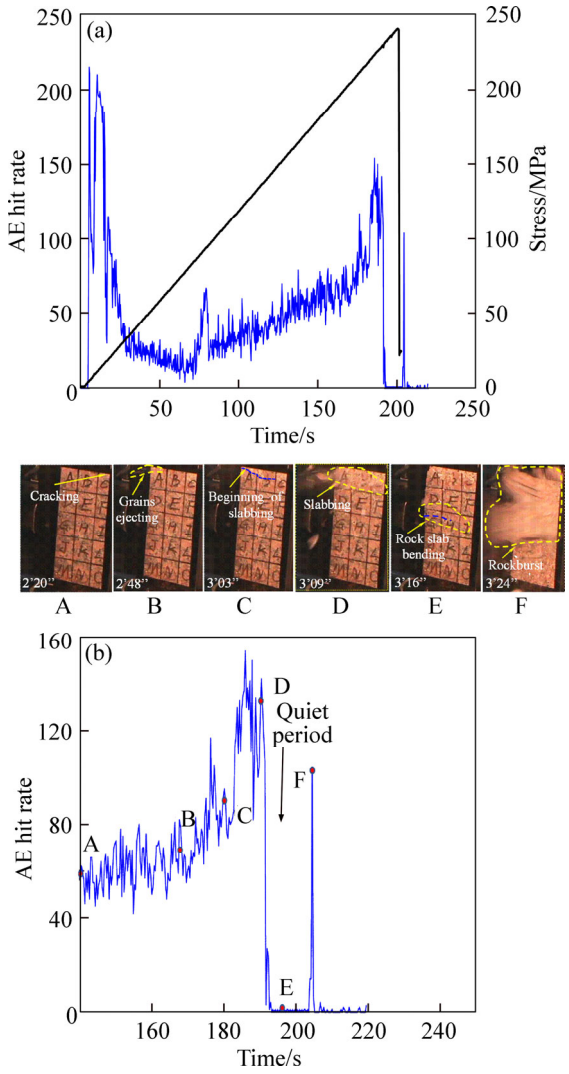

Figure 6 Results of rockburst test [7]: (a) Changes in AE hit rate with time; (b) Relationship between changes in AE hit rate and video images on free face

rock sample. During 193−203 s, the AE hit rate decreases sharply and exhibits a “quiet period”. A crack occurs in the middle of the rock slab on the free face, and the crack direction is roughly parallel to the x-direction. At 204 s, the AE hit rate increases sharply, up to 100. The slab on the free surface suddenly breaks, and the fragments are ejected violently, and sample instability occurs.

The temporal changes in the AE hit rate during the spalling test are shown in Figure 7, along with the failure phenomena recorded by the video. As shown in Figure 7, during 1−1000 s, the AE hit rate continues to decrease from the initial value of 100 to approximately 20. During 1000−2000 s, the AE hit rate maintains a relatively low level of approximately 20, but a “burst increase”, up to approximately 110, occurs at approximately 1600 s.

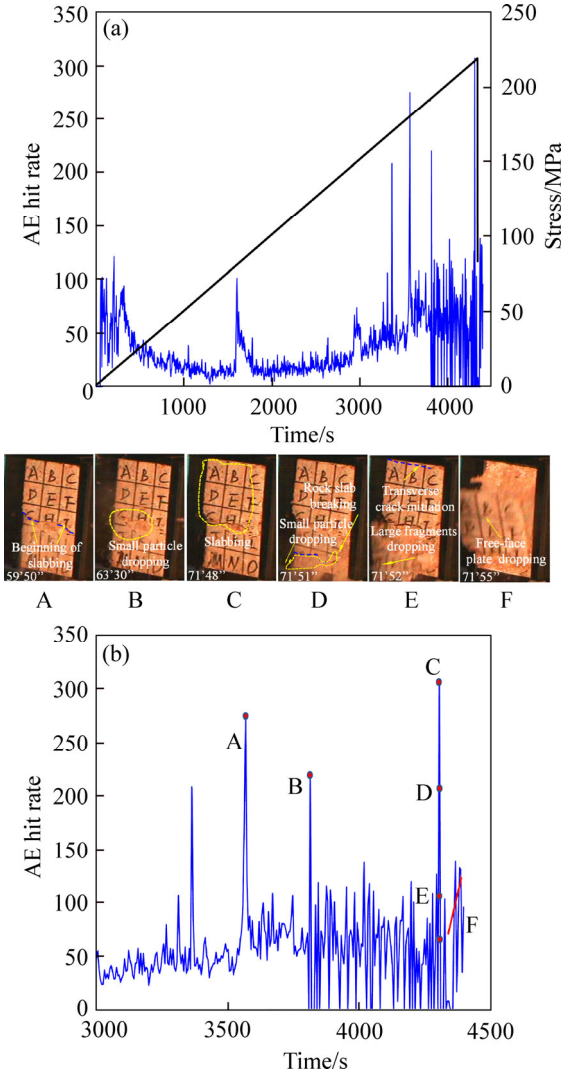

Figure 7 Results of spalling test: (a) Changes in AE hit rate with time; (b) Relationship between changes in AE hit rate and video images on free face

During 2000−3000 s, the AE hit rate increases slowly, up to 70. After 3000 s, the AE hit rate exhibits a "multi-peak" state, and the maximum rate reaches 210. At 3590 s, the AE hit rate reaches 270. In the corresponding video image, slabbing begins to appear on the free surface of the rock sample. At 4308 s, the AE hit rate reaches 300. Obvious slabbing occurs again on the free face. At 4315 s, the AE hit rate reaches 60. The rock slabs break off on the free face, and the instability of the rock sample occurs.

3.2 Amplitude evolution of AE hits during rockburst and spalling

The amplitude of the AE hits is an important characteristic parameter that represents the maximum amplitude in the attenuation waveform of the AE signals. The amplitude reflects the strength of the AE signals and can generally reflect the intensity of the fracture energy release in the rock. The amplitude evolution of the AE hits in the rockburst test is shown in Figure 8(a). It can be seen that during 1−100 s, the amplitudes of the AE hits are mostly in the range of 40−50 dB, and a few are in 50−90 dB. During 100−182 s, more AE signals are detected and are mainly concentrated in 40−70 dB. Small cracks and particle ejection occur on the free face of the rock sample. At 183 s, the amplitudes of the AE hits start to rise. Slabbing begins to occur on the free face. At 189 s, the amplitudes continue to increase, with the maximum of 85 dB. Obvious slabbing occurs again on the free surface. During 193−203 s, most of the amplitudes of the AE hits decrease sharply, and a "quiet period" occurs. A crack occurs in the middle of the rock slab on the free face, and the crack direction is roughly parallel to the *x*-direction. At 204 s, the maximum amplitude of the AE hits is approximately 80 dB. The slab on the free surface

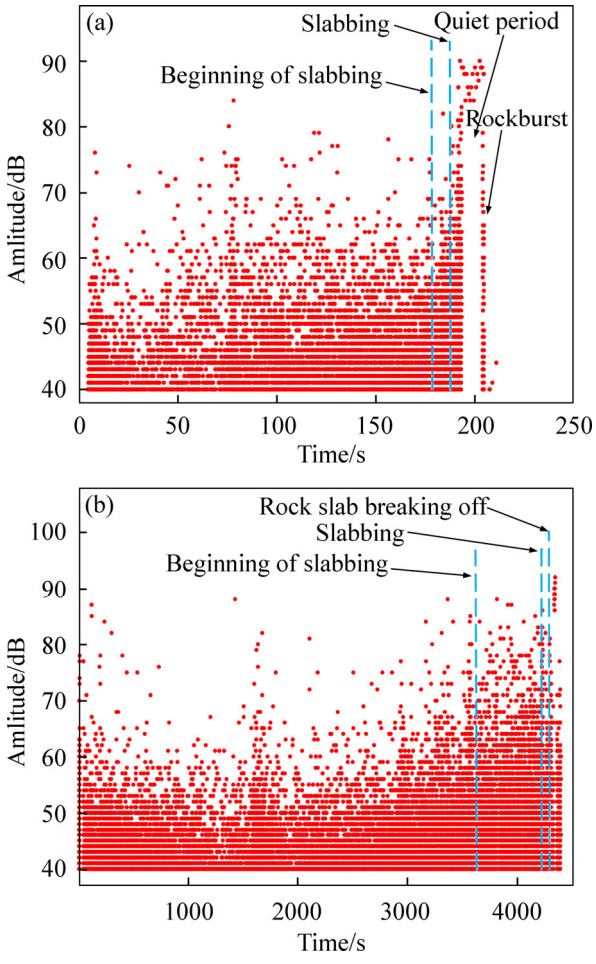

Figure 8 Amplitude evolution of AE hits during: (a) Rockburst; (b) Spalling

suddenly breaks, the fragments are ejected violently, and sample instability occurs.

The amplitude evolution of the AE hits in the spalling test is shown in Figure 8(b). It can be seen that during 1−1000 s, the amplitudes of the AE hits are mostly between approximately 40 and 55 dB and a few are between 55 and 90 dB. During 1000−2000 s, a small number of AE signals with amplitudes greater than 65 dB appear. During 2000−3000 s, more AE signals are detected and mainly concentrated between 40 and 70 dB. After 3000 s, the amplitudes of the AE hits begin to show an "upward" trend with time, and AE hits with amplitudes greater than 60 dB largely develop. At 3590 s, the maximum amplitude of the AE hits reaches 85 dB. Slabbing begins to occur on the free face of the rock sample. After that, the maximum amplitude gradually increases. At 4308 s, obvious slabbing occurs again on the face of the rock sample. At 4315 s, the maximum amplitude reaches a maximum of 93 dB. The rock slabs break off on the free face, and the instability of the rock sample occurs.

3.3 Evolution characteristics of AE hits after slabbing

From the above results, the following can be reached: 1) In the rockburst test, slabbing continued to develop after obvious slabbing appeared on the free surface. Shortly before the instability of the rock sample, the AE hit rate exhibited a "quiet period" where the AE hit rate was particularly low, and the amplitude of AE hits reached the maximum; 2) In the spalling test, the maximum amplitude of AE hits gradually increased after obvious slabbing appeared on the free. Before the instability of the sample, no "quiet period" of AE hit rate occurred. After the high-amplitude hits greatly developed, the rock slabs broke off, and instability occurred.

4 Fractal dimension evolution of AE hit number

4.1 Fractal dimension evolution of AE hit number during rockburst and spalling

Previous studies have shown that AE signals during rock failure exhibit time-fractal characteristics [28, 29]. According to the fractal geometry [30], the correlation integral $C(t)$ of the time distribution of the AE signals can be calculated as [31]:

$$C(t)=\frac{2M(t)}{M(M-1)},\ t\le T \tag{1}$$

where T is the total time of the process; t is the time interval between AE hits in the time process of T; $M(t)$ is the logarithm of the number of AE hits in time t; and M is the total number of AE hits in time range T.

The time fractal dimension D_t of the AE hit number can be calculated as [31]:

$$D_t=\lim_{t\to T}\frac{\lg C(t)}{\lg t} \tag{2}$$

According to Eqs. (1) and (2), the greater the value of D_t, the greater the change in the AE hit number, indicating that there is active fracturing inside the rock.

Figure 9 shows the temporal changes in D_t during the rockburst and spalling tests.

As shown in Figure 9(a) in the rockburst test, during 45−75 s, the value of D_t increases slowly, with the highest value being 0.2. During 76−100 s,

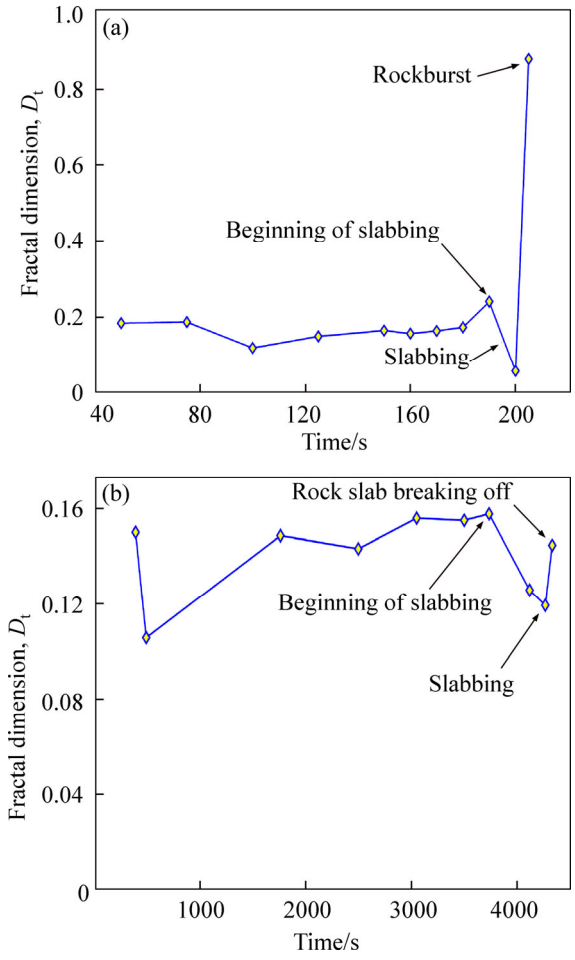

Figure 9 Temporal changes in fractal dimension evolution of AE hit number in: (a) Rockburst; (b) Spalling tests

D_t decreases slowly, with the lowest value being approximately 0.1, and after 100 s, D_t starts to increase continuously. At 183 s (beginning of slabbing), D_t increases sharply, up to approximately 0.25, and at 189 s (slabbing again), it drops rapidly. From 193 s to 203 s (the 'quiet period'), D_t drops to the minimum value of 0.08 and then rises sharply. At 204 s (instability), D_t suddenly increases to 0.88.

As shown in Figure 9(b) in the spalling test, during 1−500 s, D_t decreases from an initial value of 0.150 to 0.105. After 500 s, D_t begins to rise gradually and then declines slightly to approximately 0.13. At 3590 s (beginning of slabbing), D_t increases up to approximately 0.15 and then keeps going down. At 4308 s (slabbing again), D_t drops to the lowest value of 0.12. At 4315 s (instability), D_t increases to 0.14.

4.2 Evolution characteristics of AE hit number fractal dimension after slabbing

From the above results, the following conclusion can be reached: 1) in the rockburst test, the fractal dimension of the AE hit number continues to rise, and slabbing continues to develop after slabbing appears on the free surface. Shortly before the instability stage, the fractal dimension continues to decrease and reaches the minimum value at the end of the "quiet period", and then it suddenly increases to the maximum value when the instability occurs. 2) In the spalling test, the fractal dimension continues to decrease after slabbing appears on the free surface, and it drops to the minimum value when subsequent obvious slabbing occurs and finally increases somewhat as the slabs break.

5 AE count rate and *b*-value evolution

5.1 AE count rate evolution during rockburst and spalling

The AE count is the number of times that one signal (waveform) exceeds the present threshold within its duration [7]. The AE count rate is times in unit time that the signals exceed the present threshold. It can relate the signal (hit) and amplitude in AE tests and reflect the basic information of fracturing. Therefore, the analysis of the change characteristics of the AE count rate can help to reveal the fracture evolution inside rocks.

Figure 10 shows the temporal changes of the AE count rate during the rockburst and spalling tests.

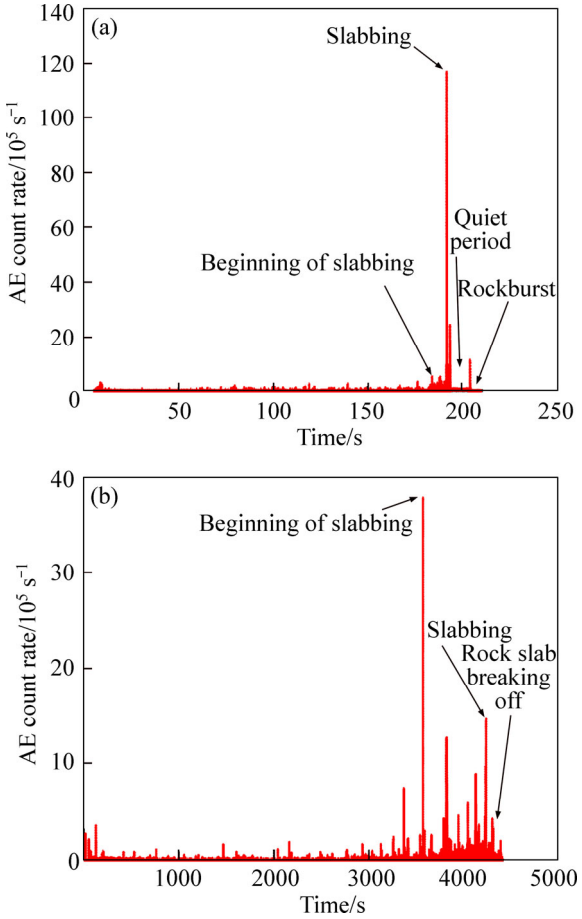

Figure 10 Temporal evolution of AE count rate in: (a) Rockburst; (b) Spalling tests

As shown in Figure 10(a), during 1−182 s of the rockburst test, the AE count rate maintains a relatively low level, approximately 2×10^5 s^{-1}. At 183 s (beginning of slabbing), the AE count rate starts to increase substantially; at 189 s (slabbing again), it reaches the maximum value of 115×10^5 s^{-1}. From 193 s to 203 s ('quiet period'), the AE count rate decreases sharply to 3×10^5 s^{-1}. At 204 s (instability), the AE count rate increases sharply, up to 10×10^5 s^{-1}.

As shown in Figure 10(b), during 1−3000 s of the slabbing test, the AE count rate maintains a relatively low level, with a maximum value of 4×10^5 s^{-1}. After 3000 s, the AE count rate gradually increases. At 3590 s (beginning of slabbing), the AE count rate increases up to 37×10^5 s^{-1}. At 4308 s (slabbing again), the AE count rate is approximately 15×10^5 s^{-1} and then keeps decreasing. At 4315 s (instability), the AE count rate drops sharply to 4×10^5 s^{-1}.

5.2 Evolution characteristics of AE count rate after slabbing

The evolution characteristics of the AE count rate after slabbing can be summarized as follows: 1) in the rockburst test, slabbing continued to develop after slabbing appeared on the free surface. Shortly before the instability, a "quiet period" characterized by low AE count rates would appear, and before that, the ring count rate increased substantially. 2) In the spalling test, the AE count rate suddenly increased and dropped when slabbing initially occurred, and it continued several times with the continued development of splitting. When subsequent slabbing occurred, the AE count rate suddenly increased and dropped, followed by multiple shocks, i.e., intermittent sudden increases. However, there was no "quiet period" until the slabs broke.

5.3 *b*-value evolution during rockburst and spalling

AE signals can be considered a kind of microseismic activity, and the rock failure process can thus be analyzed by the parameter of the *b*-value that relates the earthquake magnitude and frequency. In 1941, GUTENBERG et al [32] proposed the Gutenberg-Richter relation for the statistical relationship between the earthquake magnitude and frequency:

$$\lg N = a - bm \tag{3}$$

where m is the earthquake magnitude; N is the number of earthquakes with a magnitude in the range of Δm; and a and b are constants.

The linear least squares method was used to calculate the *b*-value of the AE hits [32]:

$$b = \frac{\sum M_i \sum \lg N_i - \Delta m \sum M_i \sum \lg N_i}{\Delta m \sum M_i^2 - (\sum M_i)^2} \tag{4}$$

where Δm, the interval of the AE magnitude, is set to 0.5 herein; and M_i is the number of AE hits within the i-th interval. Every 100 AE hits were investigated as a group.

The change in the *b*-value is closely related to the development of the cracks in the rock. An increase in the *b*-value means that the proportion of small events increases for increasing small-scale microfractures. The *b*-value changes steadily and slightly, indicating that the relative number of large events and small events is stable and that the crack developing in the rock is gradual and stable. A decrease in the *b*-value means that the proportion of large events increases, and large-scale microfractures increase. A large decrease in the *b*-value indicates that crack development changes dramatically, and failure will occur soon.

Figure 11 shows the variations in the AE *b*-value over time in the rockburst and spalling tests.

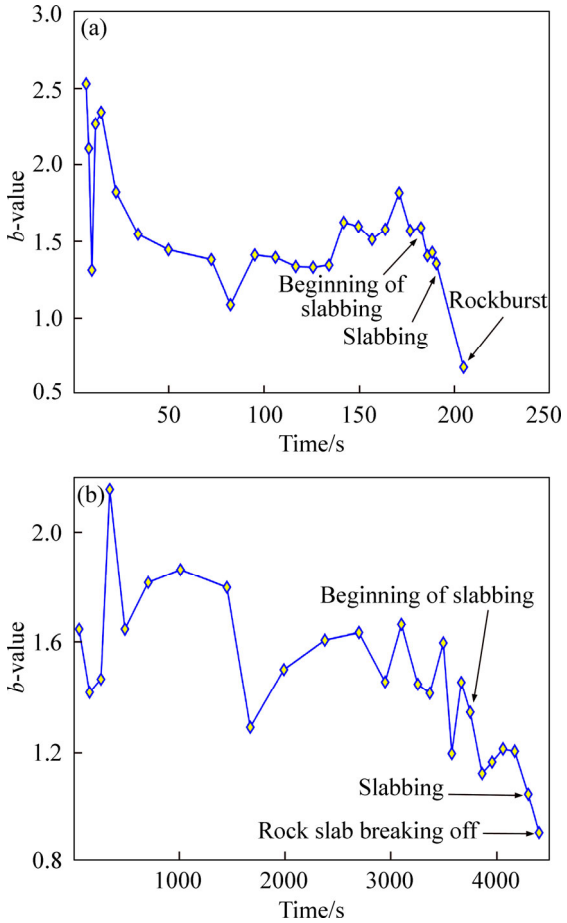

Figure 11 Variations in AE *b*-value over time in: (a) Rockburst; (b) Spalling tests

As shown in Figure 11(a), during 1−20 s of the rockburst test, the *b*-value fluctuates greatly, with a maximum value of 2.6 and the minimum value of 1.3. After 20 s, the *b*-value begins to decrease continuously to the minimum of 1.1 at 80 s. After 80 s, the *b*-value continues to increase, up to approximately 1.8 at 175 s. After that, the *b*-value begins to decrease continuously. At 183 s (beginning of slabbing), the *b*-value decreases to approximately 1.6. At 189 s (slabbing again), it decreases to 1.4, and at 204 s (instability), it decreases to a minimum of 0.6.

As shown in Figure 11(b), during 1−500 s of

the slabbing test, the *b*-value fluctuates sharply, with the maximum value of 2.2 and the minimum value of 1.4. During 500−1000 s, the *b*-value gradually increases to the maximum of approximately 1.8 and then decreases. During 1000−1600 s, the *b*-value gradually decreases to the minimum of approximately 1.2. During 1600−2700 s, the *b*-value increases from the minimum of 1.2 to approximately 1.6. After 2700 s, the *b*-value begins to fluctuate. At approximately 3600 s, the *b*-value begins to decrease continuously. At 3590 s (beginning of slabbing), the *b*-value decreases to 1.3. At 4308 s (slabbing again), the *b*-value decreases to approximately 1.1, and at 4315 s (instability), it decreases to the minimum of 0.9.

5.4 Evolution characteristics of *b*-value after slabbing

The evolution characteristics of the AE *b*-value after slabbing are as follows: 1) in the rockburst test, slabbing continued to develop after slabbing appeared on the free surface. Shortly before reaching instability, the *b*-value continued to decrease, and it decreased to the minimum value when the instability of the rock sample occurred. 2) In the spalling test, the *b*-value also kept decreasing after slabbing occurred, and it decreased to the minimum value when the rock slabs broke.

6 Dominant frequency evolution

6.1 Dominant frequency evolution during rockburst and spalling

The fast Fourier transform (FFT) is a classic spectrum analysis method for AEs [33], which can convert AE waveforms from the time domain to the frequency domain to better reflect the global frequency spectrum characteristics of signals. Using the FFT transform, the frequency amplitude of every signal can be obtained (see Figure 12).

The AE dominant frequency and amplitude evolution in the rockburst test is shown in Figure 12(a). It can be seen that during 1−50 s, the dominant frequencies are concentrated at 15−40 and 60−80 kHz, with a few signals with a low dominant frequency of approximately 10 kHz. During 50−150 s, there are four discrete dominant frequency bands at approximately 15−25, 27−45, 60−80 and 80−100 kHz, with some sporadic signals

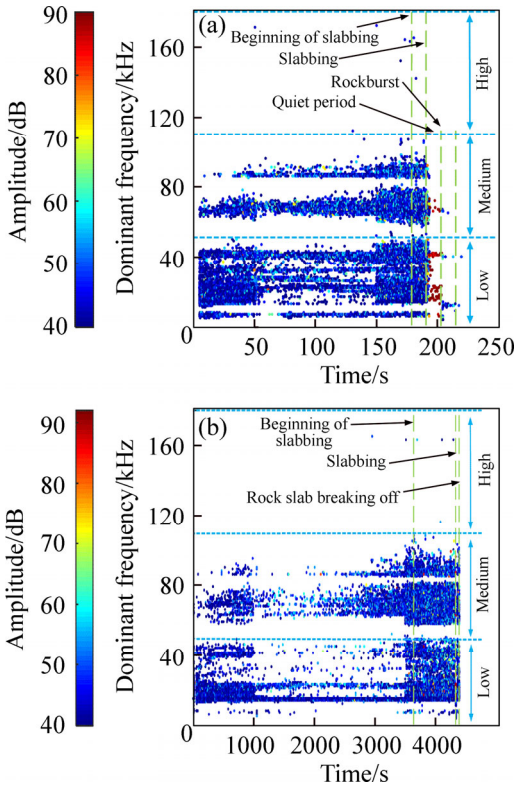

Figure 12 AE dominant frequency and amplitude evolution in: (a) Rockburst; (b) Spalling tests

with a high dominant frequency close to 160 kHz. After 150 s, the discrete dominant frequency bands form a continuous dominant frequency band, and some high-frequency hits with a dominant frequency greater than 150 kHz arise. At 183 s (beginning of slabbing), some high-frequency hits with a dominant frequency greater than 160 kHz arise. At 189 s (slabbing again), the dominant frequencies are concentrated at 15−40, 60−80 and 80−100 kHz. During 193−203 s ("quiet period"), there are a few high-amplitude hits distributed in three mid-low frequency bands, i.e., 15−20, 40−50 and 60−70 kHz. At 204 s (instability), a small number of hits appear in the low dominant frequency bands.

The AE dominant frequency and amplitude evolution in the spalling test is shown in Figure 12(b). As seen in the figure, during 1−1000 s, the dominant frequencies are concentrated in the ranges of 15−40 and 60−80 kHz, with few signals with a low dominant frequency of approximately 10 kHz. During 1000−3500 s, several discrete dominant frequency bands arise. After 3500 s, a large number of hits with low, medium and high dominant frequencies arise, and

the low-frequency and mid-frequency discrete bands develop to a continuous distribution, with a few high-frequency hits with a dominant frequency greater than 160 kHz. At 3590 s (beginning of slabbing), high-frequency hits with a dominant frequency greater than 160 kHz arise. At 4308 s (slabbing again), the dominant frequencies are concentrated in three frequency bands, i.e., 15−40, 60−80 and 80−100 kHz. At 4315 s (instability), no AEs are detected.

6.2 Evolution characteristics of dominant frequency after slabbing

Thus, the evolution characteristics of the dominant frequency after slabbing are as follows: 1) in the rockburst test, before the "quiet period", a large number of mid- and low-frequency signals arise, and there are also some high frequency hits with a dominant frequency greater than 165 kHz. During the "quiet period", a few high-amplitude and low-frequency hits appear, indicating that rockburst occurs. 2) In the spalling test, high-frequency and low-frequency signals are largely generated after slabbing begins. After the slabbing again, high-frequency hits appear. After the high-frequency hits disappeared, the rock slabs break.

7 Microcrack types evolution

7.1 Evolution of microcrack types during rockburst and spalling

Studies have shown that the rise time/amplitude ratio value and the average frequency (the ratio of the count to the duration) can be used to identify the types of microcracks in the fracture process [34]. The AE waveforms generated by tensile cracks and shear cracks are different. Generally, the waves generated by tensile cracks are longitudinal waves, exhibiting a short rise time and a relatively high frequency, whereas shear cracks generate transverse waves that propagate slowly and have a long rise time, long duration, and low frequency. Thus, AE signals with low AF and high RA values generally represent the generation or development of shear cracks. Conversely, AE signals with high AF and low RA values represent the generation or development of tensile cracks.

In this study, a critical AF/RA of 10 (i.e., k=10) was determined to differentiate shear cracks and tensile cracks (Figure 13). Then, the number and proportion of different types of microcracks could be quantified. The evolution of the types of microcracks during the rockburst and spalling test is shown in Figure 14, and the proportion evolution of the tensile and shear cracks is shown in Figure 15.

As shown in Figures 14(a) and 15(a), during

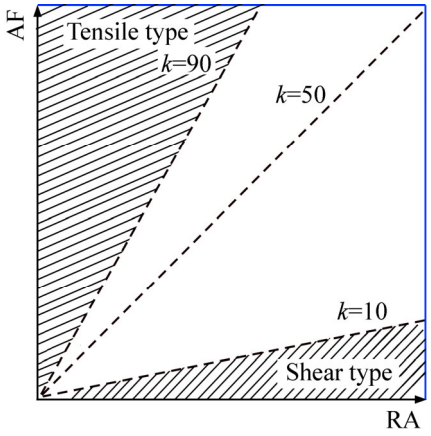

Figure 13 Schematic diagram of types of cracks based on AF/RA value

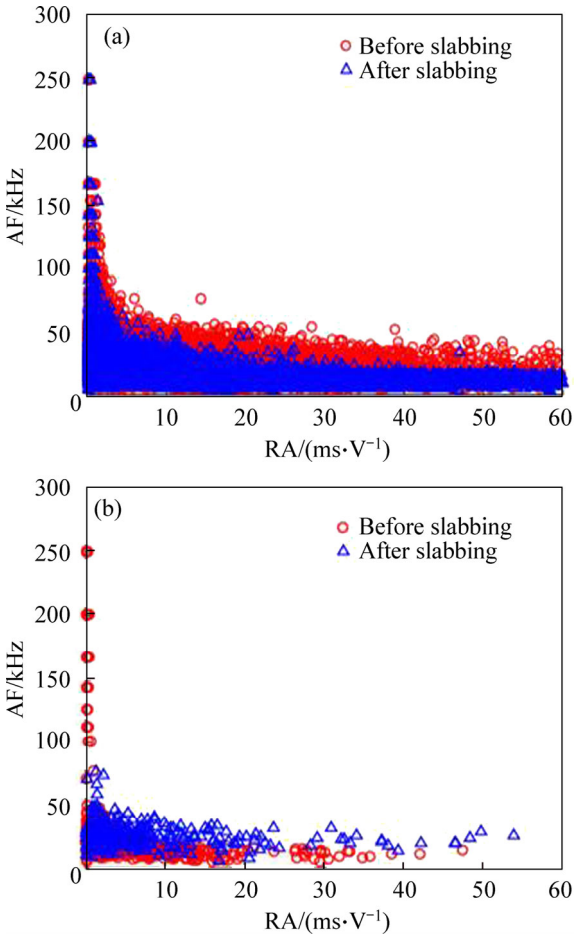

Figure 14 AF−RA distribution of AE signals in: (a) Rockburst; (b) Spalling tests

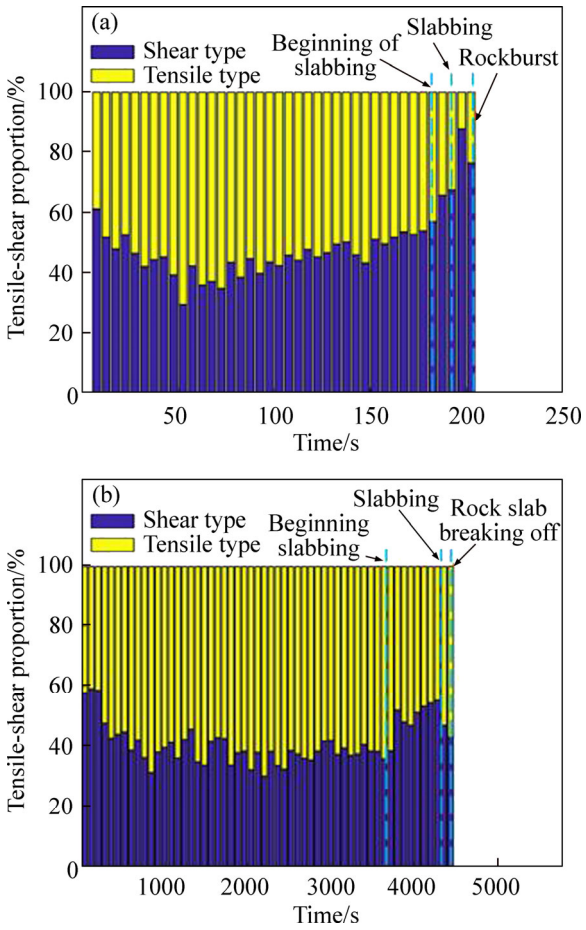

Figure 15 Tensile-shear proportion evolution of AE signals during: (a) Rockburst; (b) Spalling tests

1−50 s of the rockburst test, a small number of AE signals are detected, most of which are from tensile microcracks, accounting for 60%−70%, and others are from shear microcracks, accounting for 30%−40%. After 50 s, the proportion of the shear-type signals gradually increases, but the tensile-type signals still dominate. At 183 s (beginning of slabbing), the shear-type signals account for approximately 50%, and there are a large number of signals distributed close to the vertical axis of the AF value and the horizontal axis of the RA value before slabbing occurs. At 189 s (slabbing again), the proportion of the shear-type signals continues to increase, accounting for approximately 65%, and the signals are gradually distributed close to the horizontal axis. During 193−203 s ("quiet period"), the proportion of the shear-type signals increases sharply, accounting for approximately 90%. At 204 s (instability), the proportion of the shear-type signals increases to approximately 70%, and the signals are mainly close to the horizontal axis and exhibit a strip-shaped distribution, indicating that the rockburst failure is dominated by shear failure.

As shown in Figures 14(b) and 15(b), during 1−1000 s of the spalling test, many tensile-type signals are generated, accounting for approximately 60%−70%, and the shear-type signals account for 30%−40%. As the test progresses, the proportion of tensile-type signals gradually increases, and the signals are mainly distributed close to the vertical axis of the AF value. During 1000−3589 s, the proportions of tensile-type signals and shear-type signals are relatively stable, and the tension-type signals still dominate, accounting for approximately 60%−65%. At 3590 s (slabbing beginning), the shear-type signals account for approximately 35%, and the signals are mainly distributed close to the vertical axis. At 4308 s (slabbing again), the proportion of the shear-type signals increases, accounting for approximately 50%. At 4315 s (instability), the proportion of shear-type signals drops to approximately 45%, and the signals are still mainly distributed close to the vertical axis.

7.2 Evolution characteristics of microcrack types after slabbing

In summary, the evolution characteristics of the types of microcracks after slabbing can be summarized as follows: 1) In the rockburst test, with the continuous development of slabbing, the shear-type signals increase sharply, as well as their proportion. During the "quiet period", the shear-type signals dominate when rockburst occurs. 2) In the spalling test, slabbing continues to develop, and the proportion of the shear-type signals increase, but the tensile-type signals still dominate after slabbing occurs on the free face. When the proportion of the shear-type signals decreases, the rock slab breaks and becomes instabilities.

8 Discussion

8.1 Evolution characteristics of AE signal after slabbing

In this paper, the rockburst and spalling processes around the excavation induced by the tangential stress concentration were successfully simulated by using a self-developed true triaxial rockburst test system.

The results of the rockburst test show that after

slabbing and before the instability of the granite sample, the AE hit number and the AE count rate appear as a "quiet period" shortly before the rockburst occurs, which is consistent with results in Ref. [13]. On one hand, during the "quiet period", the rock undergoes intense shear failure, and the corresponding hits and waveforms are not easy to attenuate, which causes the "quiet period". The overlapping of the waveforms makes it difficult to detect the hits separately [14]. On the other hand, during the "quiet period", a large number of cracks develop inside the rock sample, and the cracks quickly coalesce and form macrocracks. The rock sample evolves from a relatively intact structure to a loose structure. The transverse wave (S wave) in the AE signal generally cannot propagate in the crack, so the number of AE hits drops sharply.

In addition, in both the rockburst test and the spalling test, the fractal dimension and the *b*-value of the AE hits decrease before the sample reaches instability, which is also consistent with the existing literature reports [15, 16, 20]. The decrease in the fractal dimension indicates that the proportion of the large events increases, the large-scale microfractures inside the rock sample increase, and the cracking gradually develops from disorder to order. The fractal dimension decreases to the minimum before failure, revealing that the cracks gradually coalesce and run through along the main fracture surfaces, leading to the instability and failure of the rock sample. The decrease in the *b*-value represents the great development of high-energy AE events, and the proportion of high-energy events increases for the development of large-scale fractures. Generally, the overall changes in the *b*-value during rockburst and spalling are the same or at least similar. Before rock failure, the *b*-value decreases rapidly, indicating that the proportion of the large-scale microfractures begin to increase and also the proportion of them, and the microfracture development change from disorder to order. When the *b*-value drops to the lowest value, the ruptures run through and lead to the instability failure of the rock sample.

In addition, the rockburst test shows that the dominant frequency value is low when rockburst occurs or is about to occur, which is in line with the transition of the dominant frequency to the low-frequency bands and the appearance of clear low-frequency characteristics upon rockburst failure, as indicated in Ref. [17].

It should be pointed out that the experiments in this study have revealed some new characteristics of AE results after granite slabbing. High-amplitude and low-frequency AE hits occurred during the AE "quiet period", and the proportion of the shear-type signals increased sharply and dominated before the rock slabs broke, whereas the tensile signal dominated before slabbing occurred. This was presumably because the energy release corresponding to shear fractures was high, while the energy release corresponding to tensile-splitting fractures was low. For the rockburst test, during the "quiet period", the increase in the shear proportion indicated that the creaking was dominated by the shear slippage of crystals. As the loading progressed, cracks began to intersect, forming several degradation zones inside the rock sample. The sample was severely degraded with a very low capacity. This evolved the condition for the occurrence of large-scale shear fractures. Therefore, the shear fracture dominated in the late loading stage. For the spalling test, since there were only a few microfractures in the rock, the internal cracking was relatively stable and dominated by the tensile mechanism throughout the test. The above findings are of great significance because it is known that although the "quiet period" is likely to occur before rockburst occurs, the appearance of the "quiet period" does not mean that the rockburst will certainly occur, or that the fracture will soon stop. However, if a small number of high-amplitude and low-frequency hits occur and the signals from shear fractures continue to increase during the "quiet period", the possibility of the occurrence of rockburst will be very high.

8.2 AE precursors of static and dynamic instabilities for hard rock

We explored how spalling or rockburst failure will eventually take place in the surrounding rock based on the evolution laws of AEs. Specifically, we summarized the characteristics of AEs during rockburst and static brittle failure, as shown in Table 1.

The results show that regardless of whether the rockburst or spalling ultimately occurs, both the time

Table 1 Comparison of AE precursors after slabbing and before instability

AE evolution characteristic	Rockburst	Spalling
Whether the "quiet period" appears in the AE hit rate	Yes	No
Whether the AE hit rate reaches the maximum upon instability	Yes	No
Whether the fractal dimension of AE hit number continues to decrease	Yes	Yes
Whether the AE count rate increases substantially before instability	Yes	Yes
Whether the AE *b*-value decreases rapidly	Yes	Yes
Whether the dominant frequency value reaches the minimum	Yes	No
Whether the amplitude corresponding to the dominant frequency reaches the maximum	Yes	No
Whether the proportion of the shear fractures increases	Yes	No

fractal dimension of the AE hit number and the AE *b*-value show a downward trend. The AE count rate increases sharply before the sample instability occurs. Thus, just based on these three evolution characteristics, it appears to be impossible to determine the ultimate instability mode of the rock after slabbing, whether the instability mode is due to the dynamic instability of rockburst or the static instability of slab breaking and falling.

Table 1 also shows that after slabbing, the appearance of the "quiet period", the occurrence of a small amount of AE hits with high amplitudes, and the increasing proportion of the signals from shear fractures only appear in the rockburst test but not in the spalling test. This indicates that using these three evolution characteristics can at least eliminate the possibility of spalling.

The instability mechanism of rock is complicated and can be influenced by many factors. It is indeed difficult and unrealistic to determine whether rockburst or spalling will eventually occur only based on the evolution characteristics of AEs. Comprehensive use of multiple features can help to improve the accuracy of early warning signals. The experimental investigation in this paper indicates that if obvious slabbing occurs in the surrounding rock, it is recommended to comprehensively judge the final instability mode based on multiple evolution characteristics of AE signals (see Figure 16). If the AE signals continue to appear after slabbing and the "quiet period" does not appear, static instability will possibly occur. If the "quiet period" continually appears after slabbing, a small number of high-amplitude low-frequency hits occur and the proportion of signals from shear fractures increases, the possibility of the occurrence of rockburst instability will be high, otherwise it will be low.

9 Conclusions

In this paper, rockburst and spalling instability failure in deep rock engineering was successfully simulated on granite using a true triaxial testing system. The AE evolutionary characteristics and possible different precursors were analyzed. The main conclusions are summarized as follows:

1) Regardless of whether rockburst or spalling finally occurred, both the fractal dimension of the AE hit number and the AE *b*-value showed a downward trend after slabbing, so the two

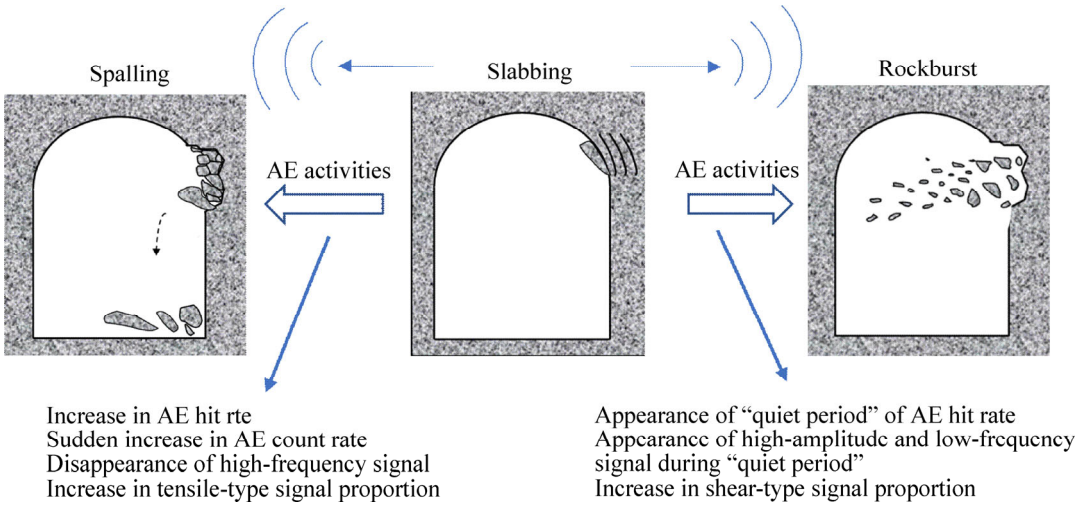

Figure 16 Schematic diagram of AE precursors of instability modes after slabbing

precursors cannot be used to predict whether the spalling or the rockburst instability mode will eventually occur.

2) The AE precursors that can be used to predict the rockburst instability are as follows: indicators such as the AE hit rate and AE count rate suddenly increase and then suddenly decrease. The AE hit rate exhibits a “quiet period”. During the “quiet period”, a small number of high-amplitude and low-frequency hits occur, and the signals corresponding to shear fractures continue to increase.

3) The AE precursors that can be used to predict the final spalling instability are as follows: both the AE hit rate and the *b*-value continuously decrease, and intermittent sudden increases appear in high frequency hits or AE count rate.

The above precursor characteristics are of great importance for the prediction and warning of geological hazards in deep rock engineering. This paper focuses on granite, and whether other types of rocks have similar precursor characteristics remaining to be determined. In addition, due to the substantial scale difference of the rock, the AE activity in the indoor laboratory can be somewhat different from that at the site. In the future, the on-site AE precursors for hard rock instability in the surrounding rock need to be studied.

Contributions

SU Guo-shao wrote the manuscript. GAN Wei set-up and performed the experiments. ZHAI Shao-bin and ZHAO Guo-fu analyzed some of the experimental data.

Conflict of interest

SU Guo-shao, GAN Wei, ZHAI Shao-bin and ZHAN Fu-guo declare that they have no conflict of interest.

References

[1] ORTLEPP W D, STACEY T R. Rockburst mechanisms in tunnels and shafts [J]. Tunnelling and Underground Space Technology, 1994, 9(1): 59−65. DOI: 10. 1016/0886-7798 (94)90010-8.

[2] LI Xi-bing, GONG Feng-qiang, TAO Ming, DONG Long-jun, DU Kun, MA Chun-de, ZHOU Zi-long, YIN Tu-bing. Failure mechanism and coupled static-dynamic loading theory in deep hard rock mining: A review [J]. Journal of Rock Mechanics and Geotechnical Engineering, 2017, 9(4): 767−782. DOI: 10.1016/j.jrmge.2017.04.004.

[3] GONG Feng-qiang, SI Xue-feng, LI Xi-bing, WANG Shan-yong. Experimental investigation of strain rockburst in circular Caverns under deep three-dimensional high-stress conditions [J]. Rock Mechanics and Rock Engineering, 2019, 52(5): 1459−1474. DOI: 10. 1007/s00603-108-1660-5.

[4] SI Xue-feng, GONG Feng-qiang. Strength-weakening effect and shear-tension failure mode transformation mechanism of rockburst for fine-grained granite under triaxial unloading compression [J]. International Journal of Rock Mechanics and Mining Sciences, 2020, 131: 104347. DOI: 10.1016/ j.ijrmms.2020.104347.

[5] HE Man-chao, MIAO Jin-li, FENG Ji-li. Rock burst process of limestone and its acoustic emission characteristics under true-triaxial unloading conditions [J]. International Journal of Rock Mechanics and Mining Sciences, 2010, 47(2): 286−298. DOI: 10. 1016/j. iJrmms.2009. 09.003.

[6] GONG Feng-qiang, WU Wu-xing, LI Tian-bin, SI Xue-feng. Experimental simulation and investigation of spalling failure of rectangular tunnel under different three-dimensional stress states [J]. International Journal of Rock Mechanics and Mining Sciences, 2019, 122: 104081. DOI: 10.1016/j.ijrmms. 2019.104081.

[7] SU Guo-shao, SHI Yan-jiong, FENG Xia-ting, JIANG Jian-qing, ZHANG Jie, JIANG Quan. True-triaxial experimental study of the evolutionary features of the acoustic emissions and sounds of rockburst processes [J]. Rock Mechanics and Rock Engineering, 2018, 51(2): 375−389. DOI: 10.1007/s00603-017-1344-6.

[8] GONG Q M, YIN L J, WU S Y, ZHAO J, TING Y. Rock burst and slabbing failure and its influence on TBM excavation at headrace tunnels in Jinping II hydropower station [J]. Engineering Geology, 2012, 124: 98−108. DOI: 10.1016/j.enggeo.2011.10.007.

[9] CHEN Bing-rui, FENG Xia-ting, LI Qing-peng, LUO Ru-zhou, LI Shao-jun. Rock burst intensity classification based on the radiated energy with damage intensity at Jinping II Hydropower Station, China [J]. Rock Mechanics and Rock Engineering, 2015, 48(1): 289−303. DOI: 10.1007/s00603-013-0524-2.

[10] PESTMAN B J, VAN MUNSTER J G. An acoustic emission study of damage development and stress-memory effects in sandstone [J]. International Journal of Rock Mechanics and Mining Sciences & Geomechanics Abstracts, 1996, 33(6): 585−593. DOI: 10. 1016/0148-9062(96)00011-3.

[11] LI C, NORDLUND E. Experimental verification of the Kaiser effect in rocks [J]. Rock Mechanics and Rock Engineering, 1993, 26(4): 333−351. DOI: 10.1007/ BF01027116.

[12] RUDAJEV V, VILHELM J, LOKAJíČEK T. Laboratory studies of acoustic emission prior to uniaxial compressive rock failure [J]. International Journal of Rock Mechanics and Mining Sciences, 2000, 37(4): 699−704. DOI: 10.1016/ S1365-1609 (99)00126-4.

[13] CHMEL A, SHCHERBAKOV I. A comparative acoustic emission study of compression and impact fracture in granite [J]. International Journal of Rock Mechanics and Mining Sciences, 2013, 64(6): 56−59. DOI: 10.1016/j.ijrmms.

2013.08.025.

[14] MORADIAN Z, EINSTEIN H H, BALLIVY G. Detection of cracking levels in brittle rocks by parametric analysis of the acoustic emission signals [J]. Rock Mechanics and Rock Engineering, 2016, 49(3): 785−800. DOI: 10. 1007/s00603-015–0775-1.

[15] TRIANTIS D. Acoustic emission monitoring of marble specimens under uniaxial compression. Precursor phenomena in the near-failure phase [J]. Procedia Structural Integrity, 2018, 10: 11−17. DOI: 10.1016/j.prostr.2018. 09.003.

[16] SELAHATTIN A, MURAT K, ABBAS T, GIANG N, HE M C. Effects of thermal damage on strain burst mechanism for brittle rocks under true-triaxial loading conditions [J]. Rock Mechanics and Rock Engineering, 2018, 51(6): 1657−1682. DOI: 10. 1007/s00603-018-1415-3.

[17] MORADIAN Z, EINSTEIN H H, BALLIVY G. Detection of cracking levels in brittle rocks by parametric analysis of the acoustic emission signals [J]. Rock Mechanics and Rock Engineering, 2016, 49(3): 785−800. DOI: 10.1007/s00603-015-0775-1.

[18] HE M C, MIAO J L, FENG J L. Rock burst process of limestone and its acoustic emission characteristics under true-triaxial unloading conditions [J]. International Journal of Rock Mechanics and Mining Sciences, 2010, 47(2): 286−298. DOI: 10.1016/j. ijrmms.2009. 09.003.

[19] HE M C, ZHAO F, CAI M, DU S. A novel experimental technique to simulate pillar burst in laboratory [J]. Rock Mechanics and Rock Engineering, 2015, 48(5): 1833−1848. DOI: 10.1007/s00603-014-0687-5.

[20] HIMURA N, SATO K, TAKAHASHI H. Fracture simulation of inhomogeneous materials and fractal characteristics of acoustic emissions and microcracks [J]. Transactions of the Japan Society of Mechanical Engineers Series A, 1994, 60(573): 1170−1175. DOI: 10. 1299/kikaia.60.1170.

[21] KONG Xiang-guo, WANG En-yuan, HU Shao-bin, SHEN Rong-xi, LI Xue-long, ZHAN Tang-qi. Fractal characteristics and acoustic emission of coal containing methane in triaxial compression failure [J]. Journal of Applied Geophysics, 2016, 124: 139−147. DOI: 10.1016/j. jappgeo. 2015.11.018.

[22] ZHANG Zhi-bo, WANG En-yuan, LI Nan. Fractal characteristics of acoustic emission events based on single-link cluster method during uniaxial loading of rock [J]. Chaos, Solitons & Fractals, 2017, 104: 298−306. DOI: 10.1016/j.chaos.2017.08.028.

[23] SU Guo-shao, FENG Xia-ting, WANG Jin-huan, JIANG Jian-qing, HU Li-hua. Experimental study of remotely triggered rockburst induced by a tunnel axial dynamic disturbance under true-triaxial conditions [J]. Rock Mechanics and Rock Engineering, 2017, 50(8): 2207−2226. DOI: 10.1007/s00603-017-1218-y.

[24] LUO Yong, GONG Feng-qiang, LI Xi-bing, WANG Shan-yong. Experimental simulation investigation of influence of depth on spalling characteristics in circular hard rock tunnel [J]. Journal of Central South University, 2020, 27(3): 891−910. DOI: 10. 1007/s11771-020-4339-5.

[25] ZHANG Zhi-zhen, GAO Feng, SHANG Xiao-ji. Rock burst proneness prediction by acoustic emission test during rock deformation [J]. Journal of Central South University, 2014, 21(1): 373−380. DOI: 10.1007/s11771-014-1950-3.

[26] JIANG Quan, YANG Bing, YAN Fei, LIU Chang, SHI Yin-gen, LI Li-fu. New method for characterizing the shear damage of natural rock joint based on 3D engraving and 3D scanning [J]. International Journal of Geomechanics, 2020, 20(2): 06019022. DOI: 10. 1061/(ASCE)GM.1943-5622. 0001575.

[27] SU Guo-shao, JIANG Jian-qing, ZHAI Shao-bin, ZHANG Gang-liang. Influence of tunnel axis stress on strainburst: an experimental study [J]. Rock Mechanics and Rock Engineering, 2017, 50(6): 1551−1567. DOI: 10.1007/ s00603-017-1181-7.

[28] ALKAN H, CINAR Y, PUSCH G. Rock salt dilatancy boundary from combined acoustic emission and triaxial compression tests [J]. International Journal of Rock Mechanics and Mining Sciences, 2007, 44(1): 108−119. DOI: 10.1016/j.ijrmms.2006.05.003.

[29] GRASSBERGER P. Generalized dimensions of strange attractors [J]. Physics Letters A, 1983, 97(6): 227−230. DOI: 10.1016/0375-9601(83)90753-3.

[30] HE Man-chao, JIA Xue-na, COLI M, LIVI E, SOUSA L. Experimental study of rockbursts in underground quarrying of Carrara marble [J]. International Journal of Rock Mechanics and Mining Sciences, 2012, 52: 1−8. DOI: 10.1016/j.ijrmms.2012.02.006.

[31] XIE He-ping, LIU Jian-feng, JU Yang, LI Jian-guang, XIE Ling-zhi. Fractal property of spatial distribution of acoustic emissions during the failure process of bedded rock salt [J]. International Journal of Rock Mechanics and Mining Sciences, 2011, 48(8): 1344−1351. DOI: 10.1016/ j.ijrmms.2011.09.014.

[32] GUTENBERG B, RICHTER C F. Frequency of earthquakes in California[J]. Bulletin of the Seismological Society of America, 1944, 34(4): 185−188. DOI: 10.1038/156371a0.

[33] TAKAI N. Digital watermarking of JPEG images by a holographic technique [C]// Proc SPIE 4829, 2003, 4829: 216−217. DOI: 10.1117/12.523972.

[34] OHNO K, OHTSU M. Crack classification in concrete based on acoustic emission [J]. Construction and Building Materials, 2010, 24(12): 2339−2346. DOI: 10.1016/ j.conbuildmat.2010.05.004.

(Edited by ZHENG Yu-tong)

中文导读

粗晶硬岩静力与动力失稳的声发射前兆

摘要：为了探究粗晶硬岩失稳的声发射前兆，采用真三轴试验系统开展花岗岩的岩爆与板裂过程的试验研究，对试验过程中岩样声发射信号进行了监测与分析，获得了岩爆和板裂试验的声发射信号在撞击数、撞击数分形维数、振铃计数率、*b* 值、主频和微破裂类型等方面的演化特征。试验结果表明，在岩板劈裂发生后，可用于预测岩样最终失稳模式为岩爆的声发射前兆是：一旦 AE 撞击数或振铃计数率等指标突然上升后又突然下降，出现“平静期”，“平静期”期间出现少量高幅值低频的撞击且剪切破裂声发射信号持续增加；可用于预测岩样最终失稳模式为板裂后折断的声发射前兆是：AE 撞击数时间分形维数、声发射 *b* 值均呈持续下降趋势的同时，出现高频撞击点或振铃计数率间歇性突增现象。

关键词：岩爆；板裂；劈裂；声发射；真三轴试验